Aero-thermodyanamic Analysis of Re-entry Capsule in Slip Flow Regime.

Harshal Gijare

me13m1028

Under the guidance of

Dr. Nishanth Dongari

भारतीय प्रौद्योगिकी संस्थान हैदराबाद
Indian Institute of Technology Hyderabad

Department of Mechanical & Aerospace Engineering

June 2015

Declaration

I declare that this written submission represents my ideas in my own words, and where ideas or words of others have been included, I have adequately cited and referenced the original sources. I also declare that I have adhered to all principles of academic honesty and integrity and have not misrepresented or fabricated or falsified any idea/data/fact/source in my submission. I understand that any violation of the above will be a cause for disciplinary action by the Institute and can also evoke penal action from the sources that have thus not been properly cited, or from whom proper permission has not been taken when needed.

(Signature)

(Harshal Gijare)

(ME13M1028)

Approval Sheet

This Thesis entitled Aero-thermodyanamic Analysis of Re-entry capsule in Slip Flow Regime. by Harshal Gijare is approved for the degree of Master of Technology from IIT Hyderabad

(Dr.B. S. Subhashchandran) External Examiner
Associate Director
DRDL

(Dr.Harish Dixit)Internal Examiner
Dept. of Mechanical & Aerospace Engineering
IITH

(Dr.Nishanth Dongari) Adviser
Dept. of Mechanical & Aerospace Engineering
IITH

Acknowledgements

I am grateful to my teacher who has taught me how to live a reponsible life with his patience and love.

I would like to express my gratitude to my guide Dr. Nishanth Dongari to allow me the freedom to work and at the same time to keep an eye to see that I do not get drifted from the main objective. I would especially like to thank him for his moral support and calmness, at the time when I have been running on low confidence with the thesis work. His honesty and humility, has always motivated us to work harder and has kept us grounded. And simultaneously, he has been the source of motivation for all our friends. Thus, the work environment, I have got to work has been vibrant and energetic.

I would like to thank Ashwani Assam for his valuable suggestion at various point of the thesis. In addition, he helped us in understanding the *OpenFOAM* software, which was the starting point for this thesis. I would also like to thank all my friends who have always maintained an atmosphere of co-operation and friendship. Thus, have made the thesis a joyful experience.

I would like to thank my guide and the entire IIT Hyderabad system for providing us an excellent computational facility to work upon.

I am expressing highest gratitude to Dr.V.K.Saraswat, who came at the point in my academic career that has boosted my interest for working in the area of high-speed gas flows involving complex practical problems.

At last I would like thank my parents for their support and patience. I know, I have failed to be with them at various moments, they would have liked me to be with them.

Abstract

We carry out numerical simulations to predict the aero-thermodynamic characteristics of a bi-conical re-entry capsule in the slip flow regime. The open source software OpenFOAM (Open Field Operation and Manipulation) is used with the compressible computational fluid dynamics (CFD) solver *rhoCentralFoam*. CFD solver is implemented with both the conventional no-slip boundary conditions, and also the first-order Maxwell's velocity slip and the Smoluchowski temperature jump boundary conditions. CFD solver has been validated with the experimental data for the pressure coefficient and density variations on the capsule surface and also validated with surface pressure and temperature and velocity for a flow over flat plate and wedge surface for altitude above 60km and Mach number above 10. The objective of the paper is to investigate the influence of rarefaction on the drag, pressure and heat transfer coefficients by comparing the conventional and slip CFD results. Comparison of bi-cone and single-cone configuration has been carried out for aerothermodyanamic optimization. It is found that bi-cone configuration is more optimized. We report results for two different altitudes of 60 km and 70 km (Knudsen numbers $(Kn) = 0.012$ and 0.037, respectively) having Mach number variation from 10 to 20, with the angle of attack varying from 0 to 20 .It is noted that the deviations between conventional no-slip CFD methods and slip CFD are small for drag and pressure coefficients, while significant for the heat transfer coefficient. Knudsen numbers are being smaller, as expected the velocity slip is at the order of 1% to 3% w.r.t. the freestream velocity. However, the normalized temperature jump is found to be very significant due to high Mach number values. This stems from the fact that non-equilibrium effects depend not merely on Knudsen number but are highly influenced by Mach number as well.

Contents

List of Figures

List of Tables

List of Symbols

Nomenclature

C_d	drag coefficient
C_h	heat transfer coefficient
C_p	pressure coefficient
e_r	rotational energy
F_d	drag force per unit area
Kn	Knudsen number
L	length scale
Ma	Mach number
p	pressure
q	heat flux
U	speed
U_x	axial velocity
U_y	radial velocity
R_n	nose radius
T	static-temperature
X	distance

Greek Letters

λ	mean free path
ρ	density
ω	viscosity–temperature index

Subscript

i	incident
o	total conditions
r	reflected
w	surface
∞	freestream condition

Chapter 1

Introduction

1.1 Literature review

A good atmospheric re-entry is when the space vehicle can withstand the extreme aerodynamic heating and make precise landing within the desired range [1]. Therefore, an accurate predictions of aero-thermodynamic loads on a re-entry capsule is imperative for aerospace applications. Thermal protection systems (TPSs) materials research largely depends on these findings [2]. For the efficient operation of hypersonic transport systems such as SpaceLiner [3], the design has to be done with optimum aerodynamic performance [4].

The need to have safe return was conceived way back in 1925 by Hohmann [5]. He developed several theoretical models for a re-entry vehicle taking into aspects factors like variable-geometry wings and external insulation. In 1946, Clauser [6] carried out a serious study of space flight. This study further explored the possibility of safe landing, but it did not take into consideration, the high-altitude atmospheric consideration, which was mostly unknown. But, now we know that presence of strong shocks, equilibrium or non-equilibrium gas chemistry, extreme temperature causing large heat fluxes are some of the flow characteristics around hypersonic vehicles. The focus of current aerospace engineers is now shifting to mimic exo-atmospheric conditions using the limited experimental data and available computational power [7]. Study of high-speed flow past the blunt body using analytical approaches has been a complex and difficult task [8].

Computational fluid dynamics (CFD) methodologies have been widely used to study complex supersonic/hypersonic flow characteristics. Efficient approaches have been developed for calculating aerodynamic characteristics of various bodies at the final segment of descent trajectory, in the continuum regime (altitude less than 40 km). Liever *et al.* [9] studied the flow solutions past Beagle-2 spacecraft mimicking the Martian environment within the continuum regime by using the CFD-FASTRAN commercial code. Mehta [10] has investigated the supersonic flow past various capsule configurations using the axisymmetric laminar-compressible time-dependent Navier–Stokes equation with a multistage Runge-Kutta equations. The use of extended Navier-Stokes equations by applying the non-equilibrium slip boundary conditions has become popular for extending the limitation of conventional CFD in the slip and transition regime of the flows. Various researchers [11, 12, 13, 14, 15, 16] have modeled the Navier-Stokes equations together with the conventional second order slip boundary conditions by incorporating the Knudsen layer phenomenon in rarefied gases. Votta *et al.* [17] have performed CFD simulations with slip boundary conditions for space re-entry vehicle using CIRA CFD code H3NS [18]. In the slip and transition flow regimes (altitude between 40 to 150 km) there is a significant scarcity for experimental data [19], especially heat transfer and temperature. Therefore, the analysis of re-entry aero-thermodynamics in these flow regimes still present a challenging problem. The Navier-Stokes equations yields inaccurate results in the slip and transitional regimes, and require special modifications for taking into account non-equilibrium effects [17, 20].

For a better aero-thermodynamic design of reentry vehicles we need data which could predict the heat and drag loads at altitude between 50 to 80 km. The vehicle need to make through the above reentry corridor (the narrow region in space that a re-entering vehicle must fly through, so that the vehicle can make a successful landing without skipping or burning out). For this we need the aerodynamic heating and drag values with varying angle of attack and Mach number, at different altitude.

1.2 Objectives

- To validate the *rhoCentralFoam* solver using first-order Maxwell's velocity slip and the Smoluchowski temperature jump boundary conditions with spalart allmaras turbulence model for different test cases with experimental data.

- To compare properties such as average and peak heat transfer and drag coefficients for bi-cone vs single-cone configuration. Decide the aerothermodynamically optimized geometry.

- To present the results of simulations carried out to measure temperature jump, velocity slip, heat load and drag forces on the capsule wall. Other thermodynamic parameters of interest are also briefly presented. Test cases cover angle of attack (AOA) from 0 to 20, Mach number from 10 to 20 and at two different altitudes of 60 and 70 km. The Knudsen number ($Kn = \lambda/L$) at altitude of 60 and 70 km is being 0.012 and 0.037, respectively. Here, λ is the gas mean free path and L is the length scale of the system.

- The major objective has been to investigate the influence of rarefaction on the drag, pressure and heat transfer coefficients by comparing the conventional CFD using no-slip boundary condition with slip CFD results.

Chapter 2

Numerical Methodology

2.1 OpenFOAM

The OpenFOAM (Open Field Operation and Manipulation) CFD Toolbox is a free, open source CFD software package which has a large user base across most areas of engineering and science, from both commercial and academic organisations. It has an extensive range of features to solve anything from complex fluid flows involving chemical reactions, turbulence and heat transfer, to solid dynamics and electromagnetics. It includes tools for meshing, notably snappyHexMesh, a parallelised mesher for complex CAD geometries, and for pre- and post-processing. Almost everything (including meshing, and pre- and post-processing) runs in parallel as standard, enabling users to take full advantage of computer hardware at their disposal.

By being open, it offers users complete freedom to customise and extend its existing functionality, either by themselves or by others. It follows a highly modular code design in which collections of functionality (e.g. numerical methods, meshing, physical models,...) are each compiled into their own shared library. Executable applications are then created that are simply linked to the library functionality. OpenFOAM includes over 80 solver applications that simulate specific problems in engineering mechanics and over 170 utility applications that perform pre- and post-processing tasks, e.g. meshing, data visualisation, etc.

The usage of Computational Fluid Dynamics (CFD) is widely spread today. As CPUs become more powerful and affordable, most larger companies in industry are using it today. However, investing in the required hardware and commercial licenses is still a hurdle for smaller businesses to use CFD. Open source softwares provide a cheap approach to simulations, compared to commercial software. However, the open source softwares are dependent on a more knowledgeable user than for the commercial softwares, as more freedom is provided with the software and documentation can be limited.

2.2 Governing equations

We solve the governing equations of fluid motion for the Eulerian phase. These equations are discretised and subsequently solved using the Finite-Volume method. The equations are expressed as a set of partial differential equations (PDEs) which are derived by the application of the laws of conservation to fluid motion.
Conservation of mass (Continuity equation):

$$\frac{\partial \rho}{\partial t} + \nabla \cdot [\overrightarrow{u}\rho] = 0 \tag{2.1}$$

Conservation of momentum neglecting gravity and particle drag:

$$\frac{\partial (\rho\overrightarrow{u})}{\partial t} + \nabla \cdot [\overrightarrow{u}(\rho\overrightarrow{u})] + \nabla p + \nabla \cdot \sigma = 0 \tag{2.2}$$

where σ is the viscous stress tensor considered positive in compression.
Conservation of energy:

$$\frac{\partial (\rho E)}{\partial t} + \nabla \cdot [\overrightarrow{u}(\rho E)] + \nabla \cdot (\overrightarrow{u}p) + \nabla \cdot (\sigma \cdot \overrightarrow{u}) = \nabla \cdot (k\nabla T) \tag{2.3}$$

where, the primary variable (ρE) is total energy of the system, k is thermal conductivity and T is temperature and $E = e + \frac{|u^2|}{2}$, where $e = c_v T = (\gamma - 1)RT$ is the specific internal energy and $\gamma = \frac{c_p}{c_v}$ is the ratio of specific heats at constant pressure and volume.
The value of temperature is calculated as:

$$T = \frac{1}{c_v}\left(\frac{\rho E}{\rho} - \frac{|u^2|}{2}\right) \tag{2.4}$$

The above four equations are closed by the ideal gas equation of state:

$$p = \rho RT \tag{2.5}$$

2.3 The *rhoCentralFoam*

The *rhoCentralFoam* segregated density based solver, is used because its proved to be a very efficient solver for high speed flow with rarified atmospheric conditions.Christopher *et al* [21] has validated this solver against various standard compressible test cases. Bansal *et al.* [22] used this solver along with *reactingFoam* (another solver within OpenFoam) for developing hypersonic flow solver. Various compressible solvers have also been compared wth *rhoCentralFoam* in literature and it is shown predict good results for high speed continuum flows [23]. We have used the 1-equation Spalart Allarmas turbulence model [24]. This model has been validated using OpenFOAM solver for atmospheric-entry capsules at subsonic speed [25]. The accuracy of the Navier-Stokes solver is improved by using the slip boundary conditions for rarefied regime of the flow. The use of Maxwell, Smoluchowski, Langmuir-Maxwell and Langmuir-Smoluchowski (so-called hybrid boundary condition) [26, 27, 28] have been incorporated in this solver [29]. The *rhoCentralFoam* using the conventional boundary conditions is referred as **no-slip**, and with the slip boundary condition is referred as **slip** throughout in this paper.

2.3.1 Algorithm for *rhoCentralFoam*

The viscous momentum and energy equations are solved using the time-splitting approach.In this approach, the inviscid equations are solved explicitly, by the 'fvc::' operator, to obtain a predicted value of the variable. Later, the diffusion terms are then introduced as implicit corrections to the original inviscid equations, represented by the 'fvm::' operator.

The solution starts with the calculation of $\rho_{f\pm}$, $T_{f\pm}$ and $u_{f\pm}$ at the face of the cell, split into outgoing and incoming directions. The face values are interpolated from the values at the cell centers and substituted in the calculation of the convective fluxes. Thereafter continuity equation is solved to obtain density, ρ. The predicted value of the velocity, $(\tilde{u})$ is calculated explicitly from the inviscid momentum equation:

$$\frac{(\rho\tilde{u}) - (\rho u^n)}{\partial t} + \nabla\cdot [u(\rho u)] + \nabla p = 0 \tag{2.6}$$

$$\tilde{u} = \frac{(\tilde{\rho u})}{\rho} \tag{2.7}$$

The value of $\tilde{u}$ is then used to calculate the corrected value of velocity at the next time step (denoted as n+1) implictly, from the viscous momentum Equation.

$$\frac{(\rho u)^{n+1} - (\rho\tilde{u})}{\partial t} - \nabla\cdot (\mu\nabla u) = 0 \tag{2.8}$$

The energy equation is solved in the similar manner. A predictor value of the energy flux $(\tilde{\rho E})$ is first calculated from the inviscid energy equation.

$$\frac{\partial(\rho E)}{\partial t} + \nabla\cdot [u(E + p)] + \nabla\cdot (\sigma\cdot u) = 0 \tag{2.9}$$

The temperature, T is obtained using Equation 2.4, which takes ρ, u and E as input. The estimated value of T is then used in the corrected energy equation:

$$\frac{\partial(\rho c_v T)}{\partial t} - \nabla\cdot (k\nabla T) = 0 \tag{2.10}$$

The pressure is then updated using the ideal gas equation of state (Equation 2.5).

2.3.2 Sutherland's viscosity model

Sutherland's law of viscosity is used to model the viscosity μ , is based on kinetic theory of ideal gases and an idealized intermolecular-force potential. Sutherland's law is still commonly used and most often gives fairly accurate results with an error less than a few percent over a wide range of temperatures.

$$\mu = \mu_{ref} \frac{T^{1.5}}{T + T_{ref}} \tag{2.11}$$

T = 110.4 K is the reference temperature. $\mu_{ref} = 1 : 716 \times 10^{-5} \frac{N.s}{m^2}$ is the reference viscosity.

2.3.3 Boundary conditions

The continuum regime of gas flows are simulated by solving the Navier-Stokes-Fourier (NSF) equations. However, experiments such as those performed by Arkilic [30] and Colin [31] have shown that the conventional NSF equations may not produce accurate results for rarefied gas flows. It is normal practice to determine the rarefaction degree of gas flows by the Knudsen number (Kn). The NSF equations applied with continuous boundary conditions of velocity and temperature are commonly known to be valid up to a Knudsen number of 0.001 if no discontinuous boundary conditions are applied [32]. However, the applicability of the NSF equations can be extended to $Kn \sim 0.1$ if non-equillibrium boundary conditions of velocity slip and temperature jump are applied [33]. A kinetic approach is ideally necessary in order to simulate gas flows with Kn numbers higher than 0.1, for example, the direct simulation Monte Carlo (DSMC).

Maxwellian velocity slip is

$$U_f - U_w = \frac{2 - \sigma_v}{\sigma_v} \lambda \frac{\partial u}{\partial y} + \frac{3}{4} \frac{\mu}{\rho T} \frac{\partial T}{\partial x}, \tag{2.12}$$

where U_f is the fluid velocity, U_w is the reference wall velocity, λ is the mean free path of gas, μ is dynamic viscocity, ρ is density of fluid, σ_v is tangential momentum accommodation coefficient and T is temperature.

Smoluchowski Temperature Jump is

$$T_f - T_w = \frac{2 - \sigma_T}{\sigma_T} \frac{2\gamma}{\gamma + 1} \frac{\lambda}{Pr} \frac{\partial T}{\partial y}, \tag{2.13}$$

where

$$Pr = \frac{\mu c_p}{k_L}, \tag{2.14}$$

where T_f is the temperature of fluid, T_w is the reference wall temperature, Pr is the non-dimensional Prandelt number, σ_T is thermal accommodation coefficient, γ is specific heat ratio, c_p is specific heat and k_L is thermal conductivity.

The *rhoCentralFoam* using the conventional boundary conditions is referred as **no slip**, and with the slip boundary condition is referred as **slip** throughout in this paper.

2.3.4 Turbulence Modelling

The prediction of flow phenomena such as boundary layer separation or shock boundary layer interaction depends strongly on the choice of the turbulence model. Algebraic models rely on equilibrium ideas to express directly the eddy viscosity in terms of known quantities of the mean flow. The well-known Baldwin Lomax model [34] has been widely used. Algebraic models are cheap, robust and require minimum requirements of computational storage and time, which used to be of great importance in the past years. But every algebraic model was built to calculate the attached turbulent boundary layers and some modifications have to be made to calculate other flow fields [35].

Two equation models, even if they sometimes have to be aware of wall distances, can be formulated independently of the flow topology and with this respect are more suited to computations of complex geometries. Moreover, they take naturally into account history effects through transport equations, and are therefore considered to be more general. However Deniaus thesis provides a classification for supersonic missile configuration and shows that some models can be difficult to implement in a general way. Moreover, boundary wall conditions are not always straightforward and can influence stability and accuracy of calculations. These numerical problems restrict their general application.

One equation models such as the [36, 37] SpalartAllmaras model provides a good compromise between algebraic and two equation models. In particular, the SpalartAllmaras model which solves directly a transport equation for the eddy viscosity, became quite popular because of its reasonable results for a wide range of flow problems and its numerical properties. So Spalart-Allmaras model is incorporated in solver. [38, 39].

Chapter 3

Validations

The *rhoCentralFoam* solver with implementation of Maxwellian slip velocity and Smoluchowski Temperature Jump boundary condition is tested with Becker's flat plate case and Lofthouse's wedge case and results compared with experimental data.

3.1 Test case-1: Becker's Flat-plate

A schematic of the boundary conditions applied in the flat plate cases is shown in Fig 3.1a. And the flow conditions in flat plate experiments , such as the Mach number, Ma, freestream temperature, T1, freestream pressure, p1 and freestream mean free path, k1, are shown in Table 3.1.A mesh independence analysis was completed to find the final mesh for the convergence solution for all the simulation cases in the present work. Here we only report the final mesh cell sizes. In the flat plate simulations, the computational results are sensitive to the numerical mesh sizes near the leading edge [29]. A typical mesh for a flat plate simulation is regular rectangular. The final mesh sizes are Dx = Dy = 0.0767 mm for Beckers case .

Case	Ma	$T_\infty(K)$	$p_\infty(Pa)$	λ_∞	$T_w(K)$	Gas
Becker	12.7	64.5	3.73	0.23	292	Argon

Table 3.1: Flow Conditions in beckers experiment

In Beckers case fig 3.2b for slip velocity shows that the DSMC data do not agree well with the experimental data, giving the lowest slip value of any of the simulations. The Maxwell/Smoluchowski conditions slightly underpredict the slip velocity. In Fig 3.2c for the surface gas temperature and pressure,only at the tip of the flat plate there is a substantial

Gas	$A_s(Pa.sK^{-1/2})$	$T_s(K)$	$R(m^2s^-2K^-1)$	γ	Pr
Argon	1.93×10^-6	142	208.1	1.67	0.67

Table 3.2: Coefficients for gas transport properties

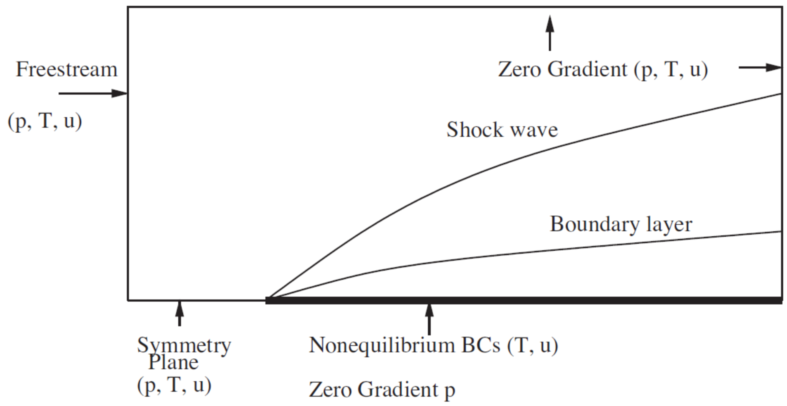

Figure 3.1: Numerical Setup for flat plate case

difference between the results of the Maxwell/Smoluchowski conditions(CFD) the DSMC data.And experimental data agrees with CFD results. Non-equillibrium effect are more pronounced at the edge of plate due to thickness of plate, so for better results at edge we need higher order boundary condition. Comparison of surface pressure agrees well for all methods this is due to the fact that, surface pressure is not governed by nonequilibrium effects as slip velocity and temperature jump does.

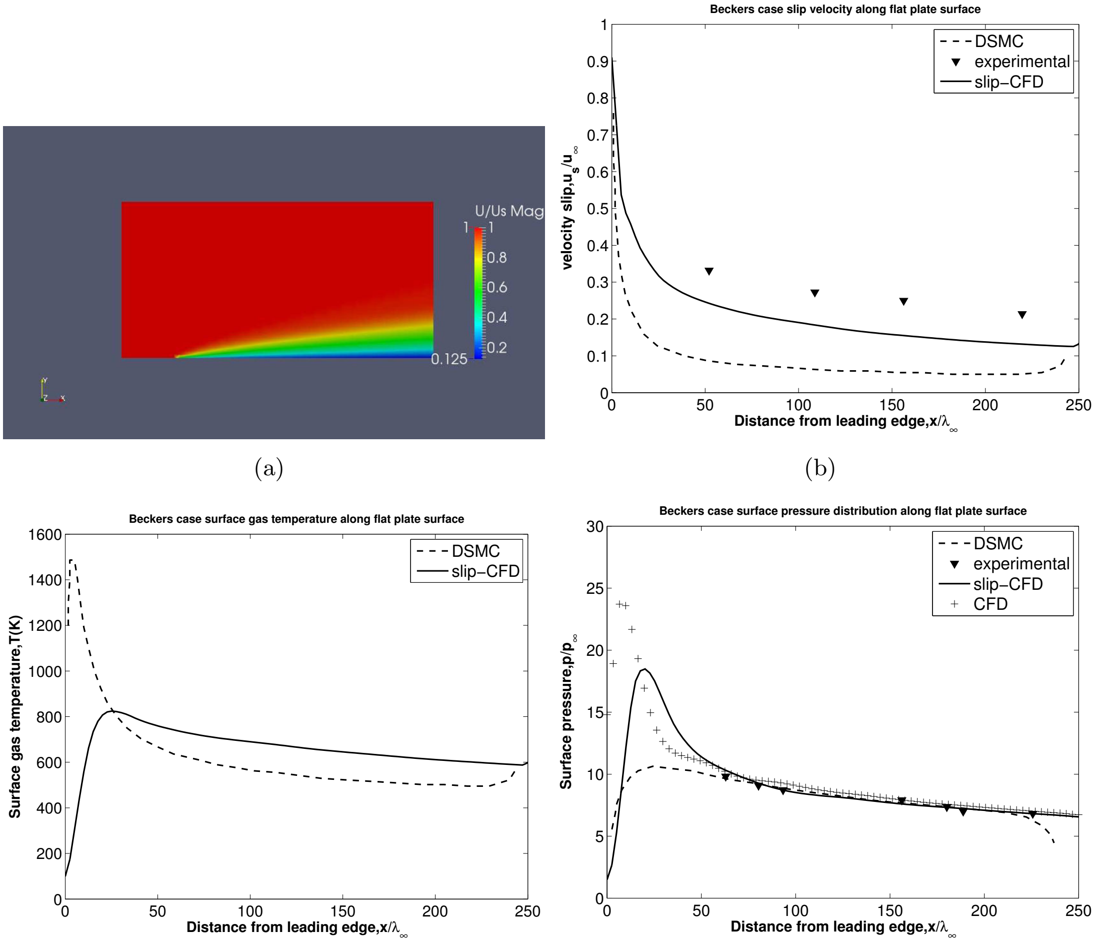

(a) (b) (c) (d)

Figure 3.2: Comparison of data values along plate length for Beckers case(a) Velocity Contours, (b)Slip Velocity along wedge surface, (c) Temperature Jump (d) Normalised pressure.

3.2 Test case-2: Lofthouse's Wedge

A schematic of the boundary conditions applied in the sharp wedgecase is shown in fig 3.3. The flowconditions and Coefficients for gas transport properties are presented in Tables 3.3 and 3.3.

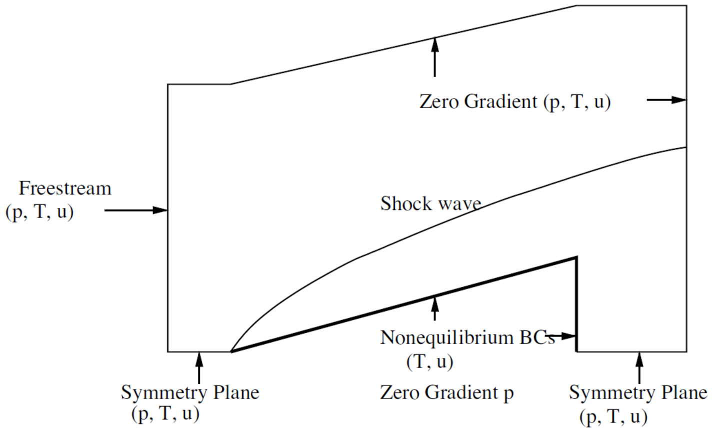

Figure 3.3: Numerical Setup for wedge case

Our computational mesh is constructed to encompass the shocks; the final mesh within the boundary layer has a linear grading in the surface-normal spacing. For the Lofthouse et al. case [40] our mesh varies over the first 120 cells near the surface, so that the final mesh size varies from 0.1 to 1.0 mm. The smallest cell size near the surface is Dx = 2.2 mm, Dy = 0.1 mm, and the mesh has around 80,000 cells.

Case	Ma	$T_\infty(K)$	$p_\infty(Pa)$	λ_∞	$T_w(K)$	Gas
Lofthouse	10	200	1.17	0.23	500	Argon

Table 3.3: Flow Conditions in lofthouse experiment

In Lofthouse case Fig 3.4b for slip velocity shows that the DSMC data do not agree well with the experimental data, giving the lowest slip value of any of the simulations. The Maxwell/Smoluchowski conditions slightly underpredict the slip velocity.In Fig 3.4c for the surface gas temperature and pressure,only at the start of the wedge there is a substantial difference between the results of the Maxwell/Smoluchowski conditions(CFD) the DSMC data.And experimental data agrees with CFD results for surface pressure. At the tip DSMC predicts better results as non-equillibrium effects are captured well in DSMC.

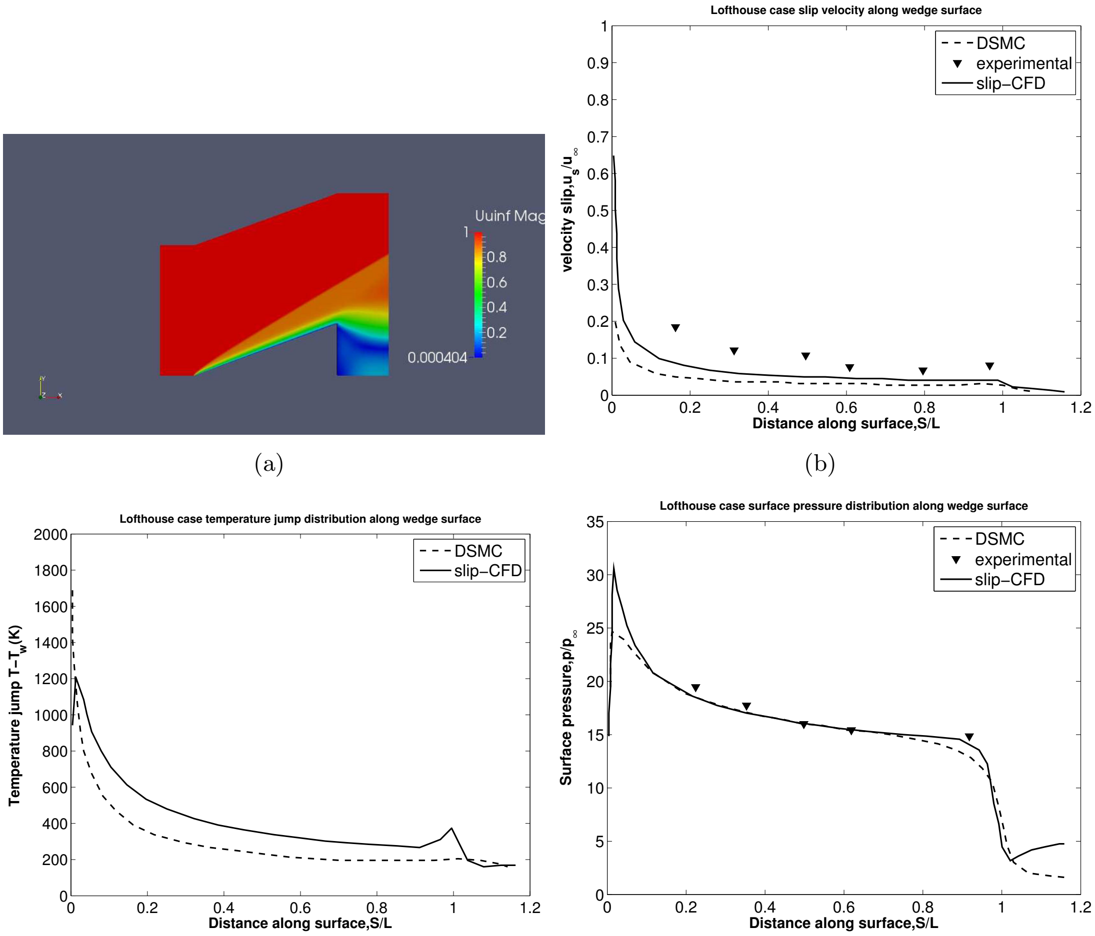

(a) (b)

(c) (d)

Figure 3.4: Comparison of data values along wedge length for lofthouse case(a) Velocity Contours, (b)Slip Velocity along wedge surface, (c) Temperature Jump (d) Normalised pressure.

3.3 Test case-3: 3D re-entry capsule)

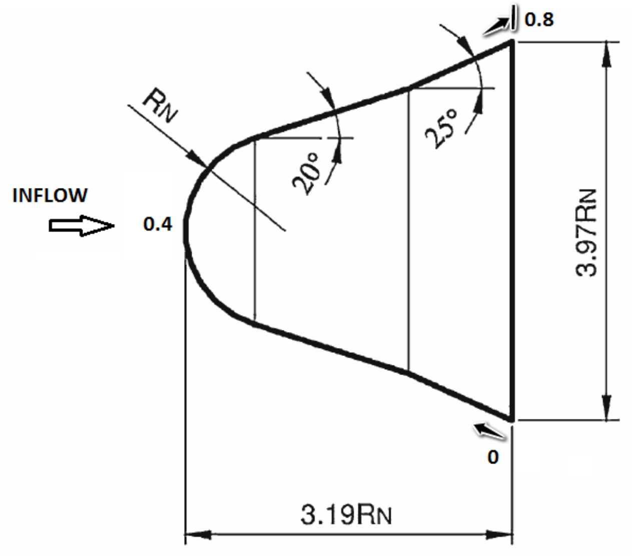

Figure 3.5: Re-entry vehicle model

A complex geometry, similar to ballistic reentry capsule has been considered for numerical simulation. This vehicle configuration consists of a blunt bi-cone with 20/25 degree cone angles. Total length is 3.19 and base diameter 3.97 times the nose radius as shown in Fig 3.5. Three dimensional grid of million of cells is used for the present simulations . The freestream pressure and temperature are 833Pa and 63 K, respectively. Freestream Mach number of 5.0 with angle of attack of 4.66 is considered in the present computation.

The flow features like bow shock and the effect of second cone are clearly captured as shown in density contour plot over the reentry configuration Fig 3.6c and it agrees with AUSM results in [41]. Comparison of wind tunnel test data [42] and AUSM [41] method with current solver for coefficient of pressure and density over the surface of reentry configuration is shown in Fig 3.6a and Fig 3.6b . The results from both the CFD methods have good agreement with the experimental data. In addition we notice that both the slip and no-slip CFD methods coincide with each other as the result corresponds to the continuum regime ($\approx$ 33 km). Higher pressure is observed on windward side than leeward side. Maximum pressure is observed at the stagnation point or nose of the capsule and pressure remains constant along the surface of capsule till the second cone. A jump in the pressure is observed at the second cone due to the formation of weak shock wave formation. Pressure coefficient is closely matched with the wind-tunnel data near nose of the capsule. Density plots results also agrees well with the experimental data.

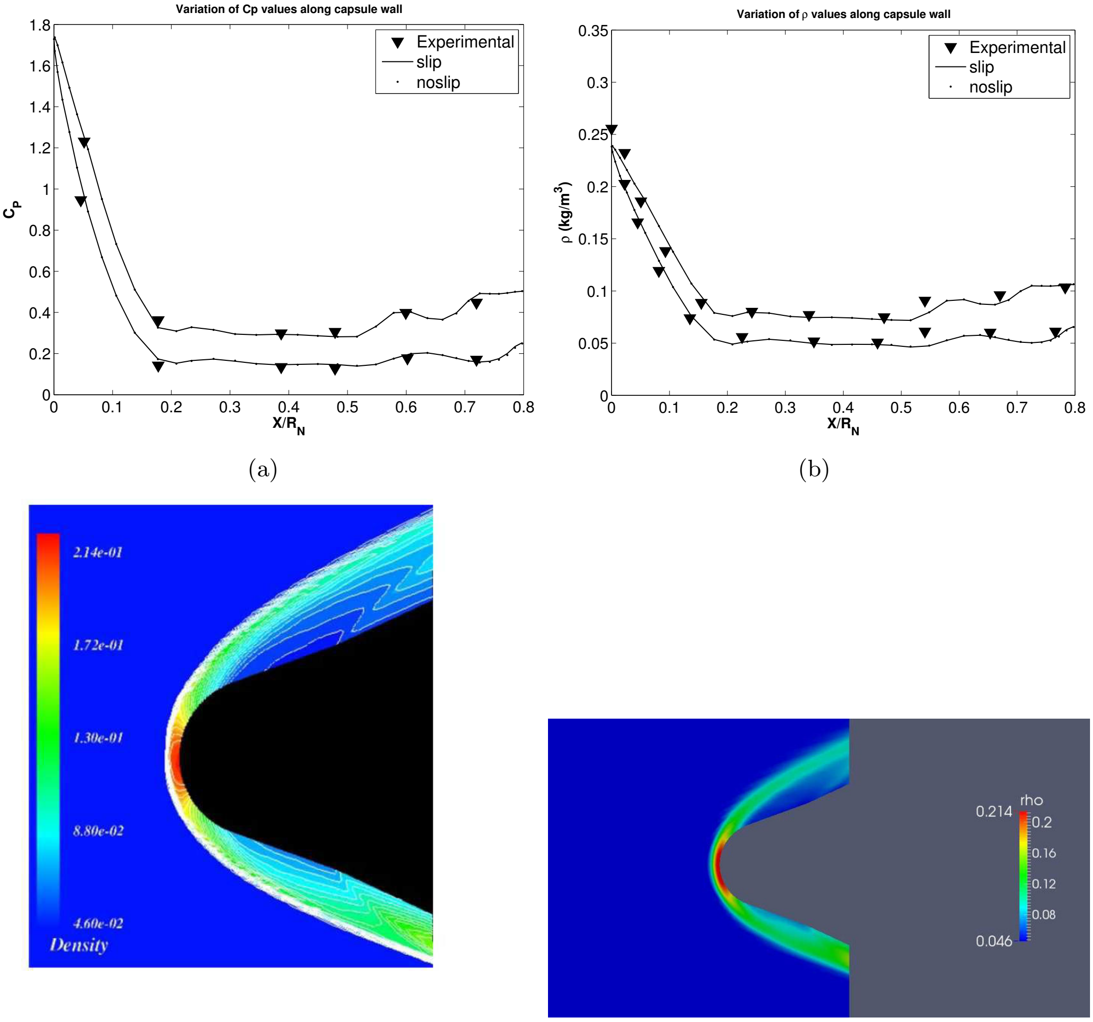

(a)

(b)

(c)

(d)

Figure 3.6: Comparison of data values along capsule wall between CFD and experimental and AUSM (a) C_p coefficient of pressure, (b) density, (c) Density contours using AUSM scheme (d) Density contours using OpenFOAM.

Chapter 4

Single-cone vs Bi-cone

A bi-cone and a single cone ballastic re-entry capsules have been considered in the current study. Bi-cone re-entry capsule is chosen for which experimental data is available and same is validated in section 3.3. For single cone re-entry capsule, first cone angle, total length and nose radius is kept same, first cone angle as 20, total length 3.19 times nose radius, and nose radius $R_n = 0.1$ m for current investigation. Results for aerothermodyanamic coefficients are compared below at 0^0 angle of attack. Based on the comparison between single-cone and bi-cone geometry for heat Transfer Coefficient and drag Coefficient optimum geometry can be decided.

4.1 Results and Discussion

The drag coefficient C_d along a surface is a measure of net kinetic energy flux of the molecule impinging on the surface, which is defined as follows

$$C_d = \frac{F_d}{\frac{1}{2}\rho_\infty U_\infty^3}, \tag{4.1}$$

Where F_d is the drag force per unit area, and U_∞ are the freestream density and velocity receptively. Coefficient of heat transfer C_h along a surface is a measure of net energy flux of the molecule impinging on the surface. It is defined as follows,

$$C_h = \frac{q_w}{\frac{1}{2}\rho_\infty U_\infty^3}, \tag{4.2}$$

Where q_w is the heat flux ρ_∞. Comparison of C_d at different altitudes and at different Mach numbers is shown in Fig. 4.1. Peak value of drag coefficient for both configurations is identical in every case. But after formation of second shock wave, the value of drag coefficient is more for bi-cone configuration. Looking at tabel 4.1, The deviation of average value of drag coefficient for bi-cone w.r.t single-cone configuration is well below 5%, and it reduces with increase in altitude. In practical scenario the drag coefficient value effects the accuracy in safe landing of the capsule. Lower the value of drag coefficient higher is the accuracy in landing.

Fig. 4.2 demonstrates comparison of heat transfer coefficient. Plot shows that peak value of heat transfer coefficent is reduced significantly for bi-cone configuration and the deviation is around 40%. The value of local heat transfer coefficient is higher for single-cone configuration on the entire capsule. Looking at tabel 4.2 The deviation of average value of heat transfer coefficient over entire capsule for bi-cone configuration w.r.t single-cone, value of deviation is around 15% - 35%. So we can say heat flux acting on capsule is reduced much when configuration is changed from single to bicone.C_h value plays key role in determining the insulation/ablation layers on the capsule, i.e. So weight of the overall system is reduced and safty in landing increased. Hence by observing both drag and heat transfer coefficients bi-cone configuration is aerothermodyanamically better optimized compared to single cone case.

Cd	**60km**			**70km**		
Speed	**3000 m/s**	**4500m/s**	**6000m/s**	**3000 m/s**	**4500m/s**	**6000m/s**
Single-cone	0.657	0.640	0.635	0.669	0.647	0.639
Bi-cone	0.679	0.663	0.657	0.685	0.666	0.658
%Deviation	3.36	3.54	3.47	2.48	2.85	3.03

Table 4.1: Average drag coefficient C_d data at 60 km and 70 km altitude for various flow conditions. Here, absolute values are presented for Single-cone and Bi-cone configurations. Deviation denotes the % of deviation of bi-cone with single-cone configuration results.

Ch	**60km**			**70km**		
Speed	**3000 m/s**	**4500m/s**	**6000m/s**	**3000 m/s**	**4500m/s**	**6000m/s**
Single-cone	0.014	0.012	0.011	0.037	0.036	0.036
Bi-cone	0.1	0.008	0.007	0.032	0.03	0.029
%Deviation	29.19	32.39	34.54	15.56	18.41	19.74

Table 4.2: Average heat transfer coefficient C_h data at 60 km and 70 km altitude for various flow conditions. Here, absolute values are presented for Single-cone and Bi-cone configurations. Deviation denotes the % of deviation of bi-cone with single-cone configuration results.

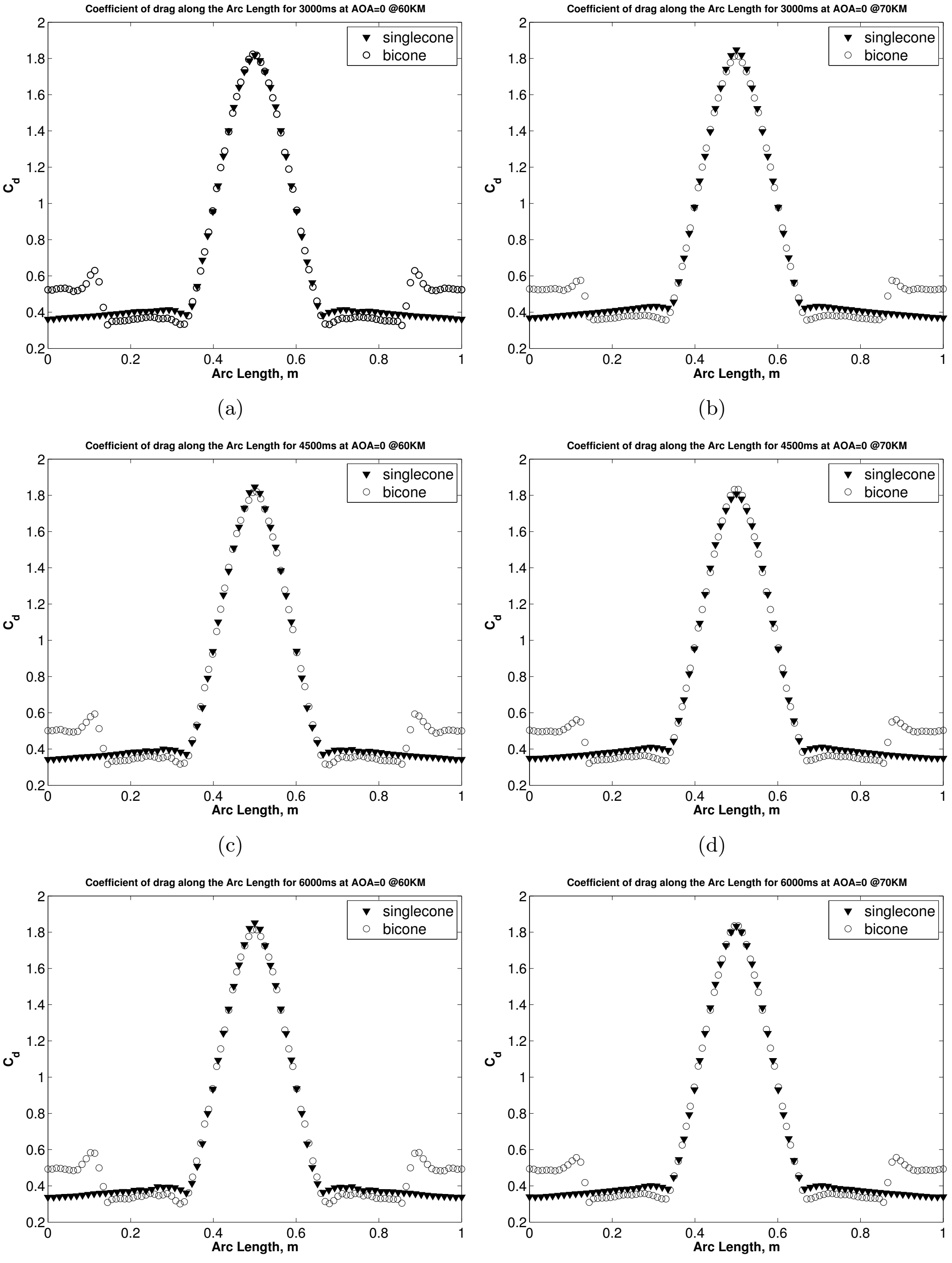

(a) (b)

(c) (d)

(e) (f)

Figure 4.1: Comparison of drag coefficient (C_d) variations on the capsule surface between Single-Cone and Bi-Cone geometry. Here, the arc length 0 is located at the downstream of the windward side and 0.783 for Single-Cone and 0.795 for Bi-Cone at the downstream of the leeward side. Here, all left side (a, c and e) subplots are for 60 km altitude condition, while the right ones (b, d and f) are for 70 km condition.

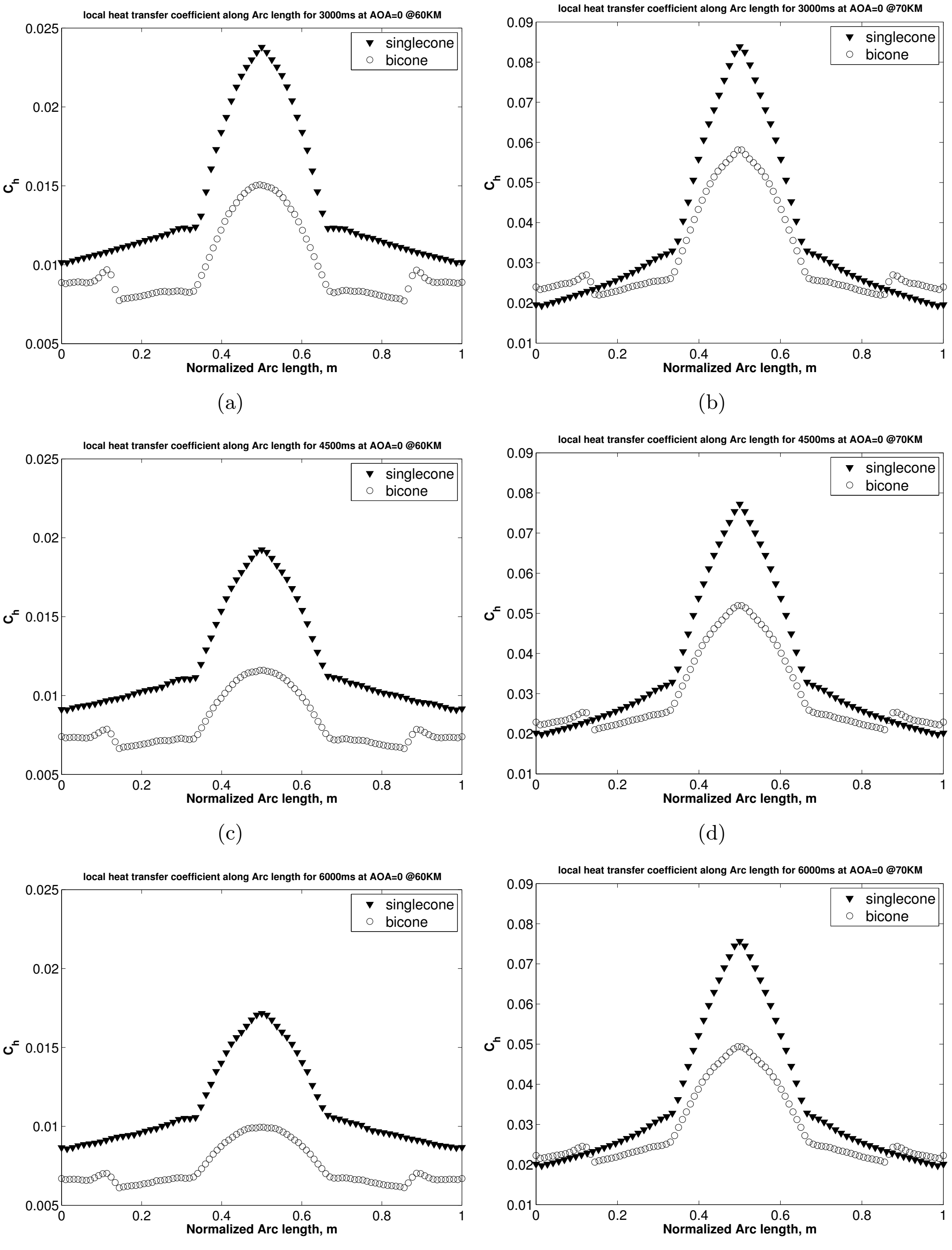

(a) (b)

(c) (d)

(e) (f)

Figure 4.2: Comparison of heat transfer coefficient (C_h) variations on the capsule surface between Single-Cone and Bi-Cone geometry. Here, the arc length 0 is located at the downstream of the windward side and 0.783 for Single-Cone and 0.795 for Bi-Cone at the downstream of the leeward side. Here, all left side (a, c and e) subplots are for 60 km altitude condition, while the right ones (b, d and f) are for 70 km condition.

Chapter 5

Analysis of Bi-Cone Capsule

We have carried out the parametric study for the 2D geometry for the ballistic reentry capsule described previously. The parameters varied are Altitude - 60 and 70 KM, angle of attack AOA $= 0, 10, 16, 20$ degree and speed $|V| = 3000, 4500, 6000$ m/s. Simulations are carried out for two different solvers one is density based compressible solver and another is same solver with extended CFD using non-equilibrium boundary conditions. Results are then compared.

We studied slip velocity and temperature jump at capsule wall and these two parameters are plotted vs arc length. And also normalized density, coefficient of local heat transfer C_h, and drag coefficient C_d are calculated along wall. And at the end averaged value over entire capsule surface is compared with noslip CFD solver results.

5.1 Mesh Independence Study

We have carried out mesh independent study for current geometry using 3 different mesh using 40000, 60000, 100000 cells, refer (Figure Fig. 5.1). It shows that mesh with 40000 cells shows slight deviation for temperature jump from 60000 and 100000 cells, but both axial and radial sleep velocities are not varying with mesh. For temperature jump there is not significant difference for 60000 cells and 100000 cells mesh. So We chose the mesh with 60000 cells Figure Fig. 5.2 shows the mesh used for all simulation, mesh is fine near wall and coarse in outer domain.

5.2 Effect of Rarefaction on Aerothermodyanamics

5.2.1 Normalized Density

Normalized density (ρ/ρ_∞) is the ratio of density around capsule wall with atmospheric density (Static Condition). Noramlized density (ρ/ρ_∞) variation on the capsule surface is demonstrated in the Fig. 5.3. Shocks at the beginning of the second cone on the windward

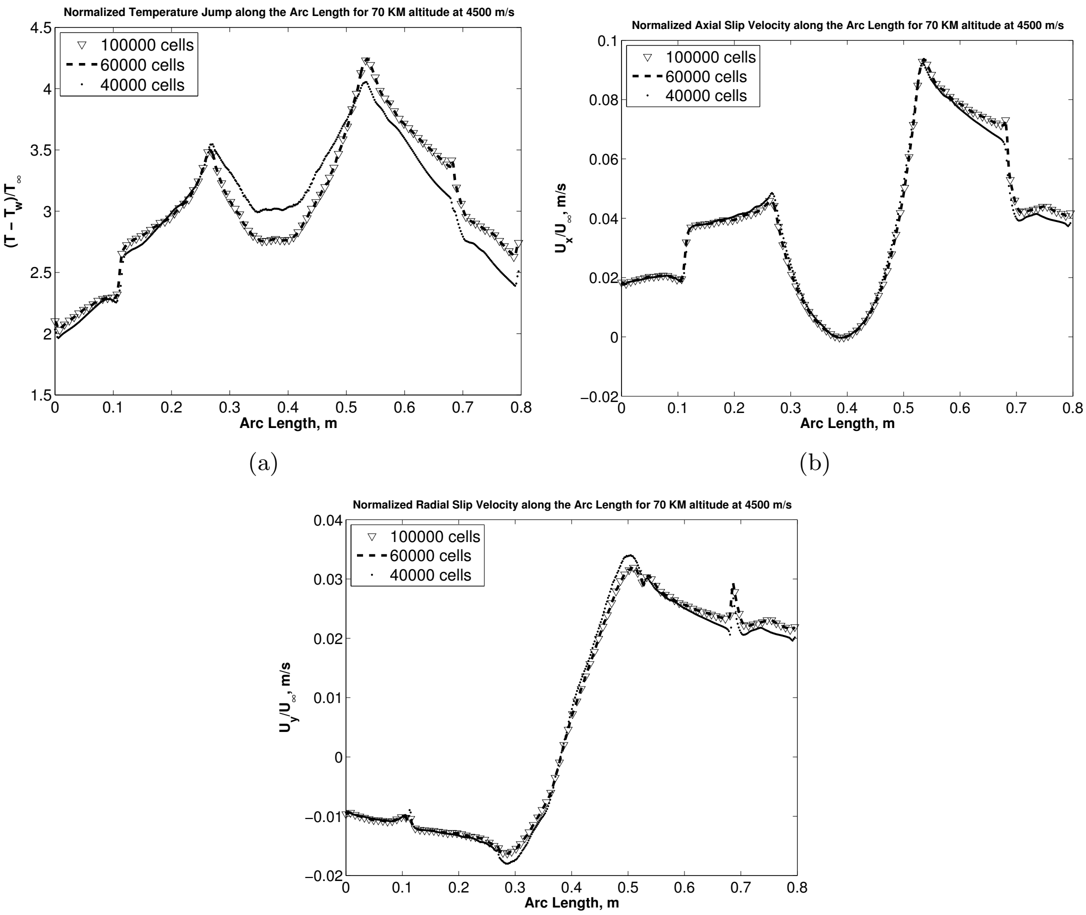

(a) (b)

(c)

Figure 5.1: Mesh Independance Check

(arc length of 0.1m) and on the leeward (arc length of 0.7m) side can be seen in all subplots of Fig. 5.3. As the angle of attack increases, on the windward side and the nose region, the slip velocity decreases (see Fig. 5.7). This results in increase in the density value in these regions of the capsule. The no-slip CFD method over predicts the slip CFD method for all conditions, as the flow is brought to rest on the capsule wall due to the imposition of no-slip boundary. As the freestream speed increases the deviation between no-slip and slip increases, at 3000 m/s the difference between them is very low but at 6000 m/s its very high and also peak value of normalized density is higher at higher Mach number. This is because particles are brought to rest from high speed to very low speed in same region. And as altitude increase (Away from continuum region) we can see peak value of normalized density decreases as expected but deviation increases with increase in altitude, as non-equillibrium effects are more pronounced at higher altitude. So noslip results will differ from slip boundary condition results as altitude increases.

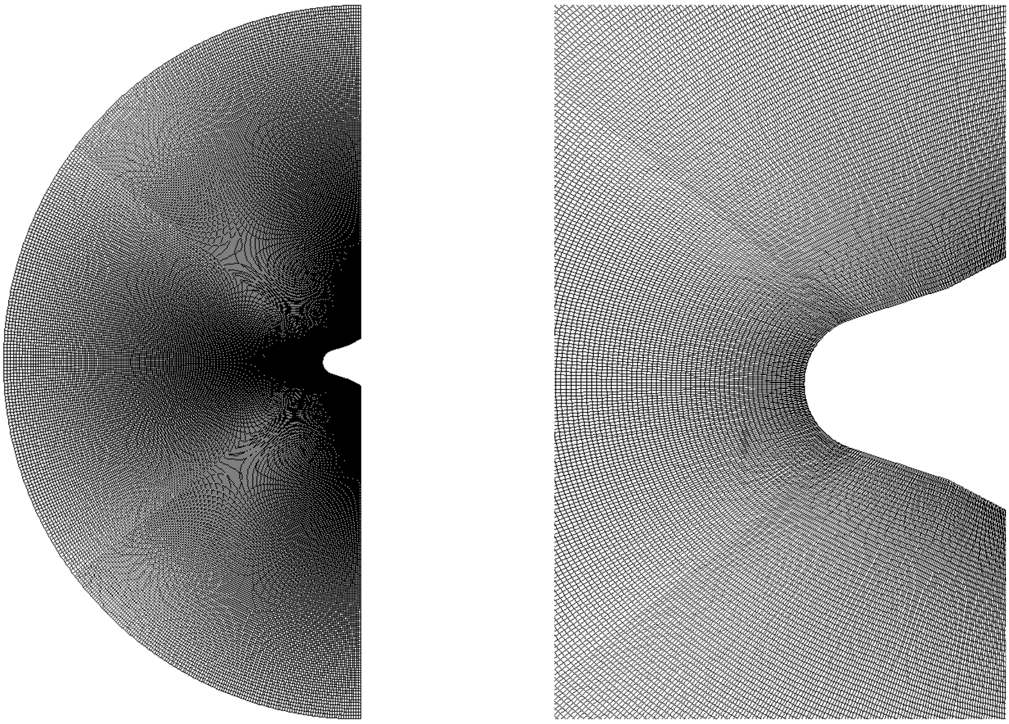
(a) (b)

Figure 5.2: Mesh with 60000 cells and aspect ratio 10 (a) Complete Mesh (b) Zoomed near capsule wall.

5.2.2 Drag Coefficient

Method to calculate drag coefficient is mentioned in section 4.1. Drag force consists of two components, which are drag due to pressure difference and drag due to friction between fluid layer and solid objects. And in case of flow over a re-entry capsule drag force mainly consists of pressure drag component. Drag coefficient (C_d) variation on the capsule surface is demonstrated in the Fig. 5.4. As angle of attack increases, density is increasing on windward side and it decreases on leeward side. Also after second shock, density is rising on windward side so drag coefficient is. And also increasing angle of attack results in increase of pressure drag component on windward side. Peak value of drag coefficient is not affected with altitude or Mach number. As we can see values of drag coefficient are very close for slip and noslip conditions in each case as value of pressure is not affected with non-equillibrium effects. So amount of deviation is present only due to frictional drag contribution. (table 5.1) We can see the percentage deviation from table its below 1% in almost every case.

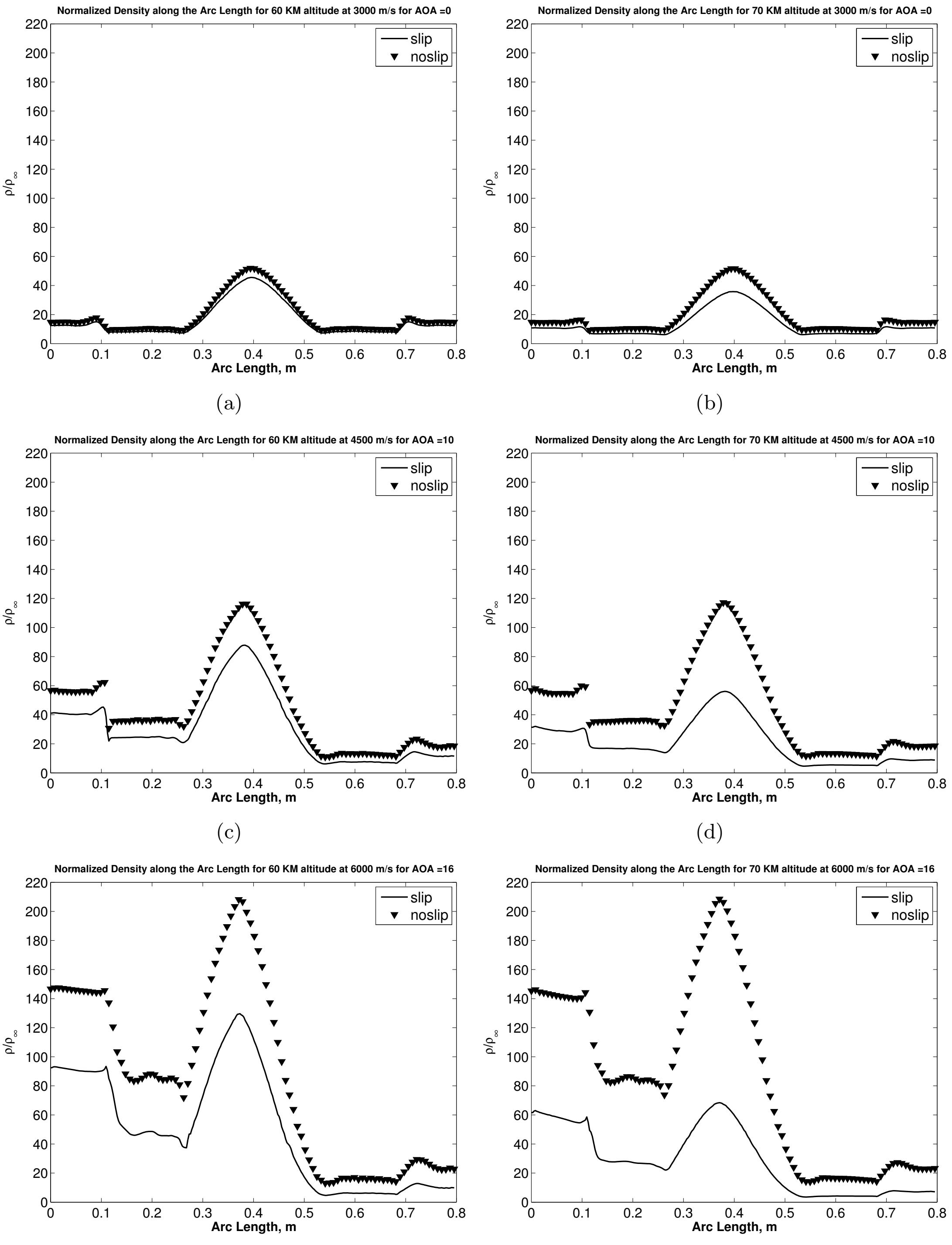
Normalized Density along the Arc Length for 60 KM altitude at 3000 m/s for AOA =0

Normalized Density along the Arc Length for 70 KM altitude at 3000 m/s for AOA =0

Normalized Density along the Arc Length for 60 KM altitude at 4500 m/s for AOA =10

Normalized Density along the Arc Length for 70 KM altitude at 4500 m/s for AOA =10

Normalized Density along the Arc Length for 60 KM altitude at 6000 m/s for AOA =16

Normalized Density along the Arc Length for 70 KM altitude at 6000 m/s for AOA =16

(a) (b)

(c) (d)

(e) (f)

Figure 5.3: Normalized density comparison on the capsule surface at different altitudes with variation of speed for different angles of attack (a) Variation of at 60km and 3000m/s. (b) 70km and 3000m/s. (c) 60km and 4500m/s (d) 70km and 4500m/s (e) 60km and 6000m/s (f) 70km and 6000m/s

%Deviation - Coefficient of drag				
60km				
Angle of attack	0	10	16	20
3000(m/s)	0.0156	0.04688	0.0156	0.0620
4500(m/s)	0.0470	5.0501	0.0153	0.6958
6000(m/s)	0.0901	0.3966	0.1373	2.2887
70km				
Angle of attack	0	10	16	20
3000(m/s)	0.2071	0.1654	0.2134	2.2121
4500(m/s)	0.2350	0.2164	0.1840	0.2813
6000(m/s)	0.3476	0.6711	0.3909	24.7745

Table 5.1: Percentage deviation in Coefficient of Drag

5.2.3 Heat Transfer Coefficient

Method to calculate heat transfer coefficient is mentioned in section 4.1. Heat transfer coefficient (C_h) variation on the capsule surface is demonstrated in the Fig. 5.5. It demonstrates the variation of C_h along the arc length on the capsule surface. Significantly higher values of C_h are predicted on the windward and nose portion of the capsule by slip method when compared to noslip method. At the stagnation point, the value is significantly high for slip CFD method.

At stagnation point, properties are found to be in equilibrium nature, as the agreement between slip CFD and no-slip CFD methods is very good, and this particular observation for C_h comparison is very interesting in contrast to the C_d predictions. This may be due to the fact that non-equilibrium nature of momentum transfer (C_p and C_d) is simply governed by the Knudsen number, while the non-equilibrium effect for energy transfer is a combination of both Knudsen and Mach numbers. For both the 60 km and 70 km altitude conditions, Knudsen numbers are relatively lower, and C_p and C_d predictions observe minute deviations between the slip CFD and no-slip CFD methods. However, the non-equilibrium nature for temperature/heat predictions are significantly influenced by the Mach number as discussed above. Looking at the average values reported in (table 5.2) we can see deviation is increasing with Mach number and altitude. With altitude deviation increases because at 70 km its more deviated from continuum. Maximum deviation reported is around 37% is significantly high. So it's proved that N-S equation along with non-equillibrium boundary conditions gives better results compared to just N-S equation with conventional no-slip boundary condition. Hence for better results, the CFD methods require not only higher-order slip/jump boundary conditions, but also the non-linear constitutive relations in the governing equations to improve their applicability for rarefied and high Mach number flows such as re-entry.

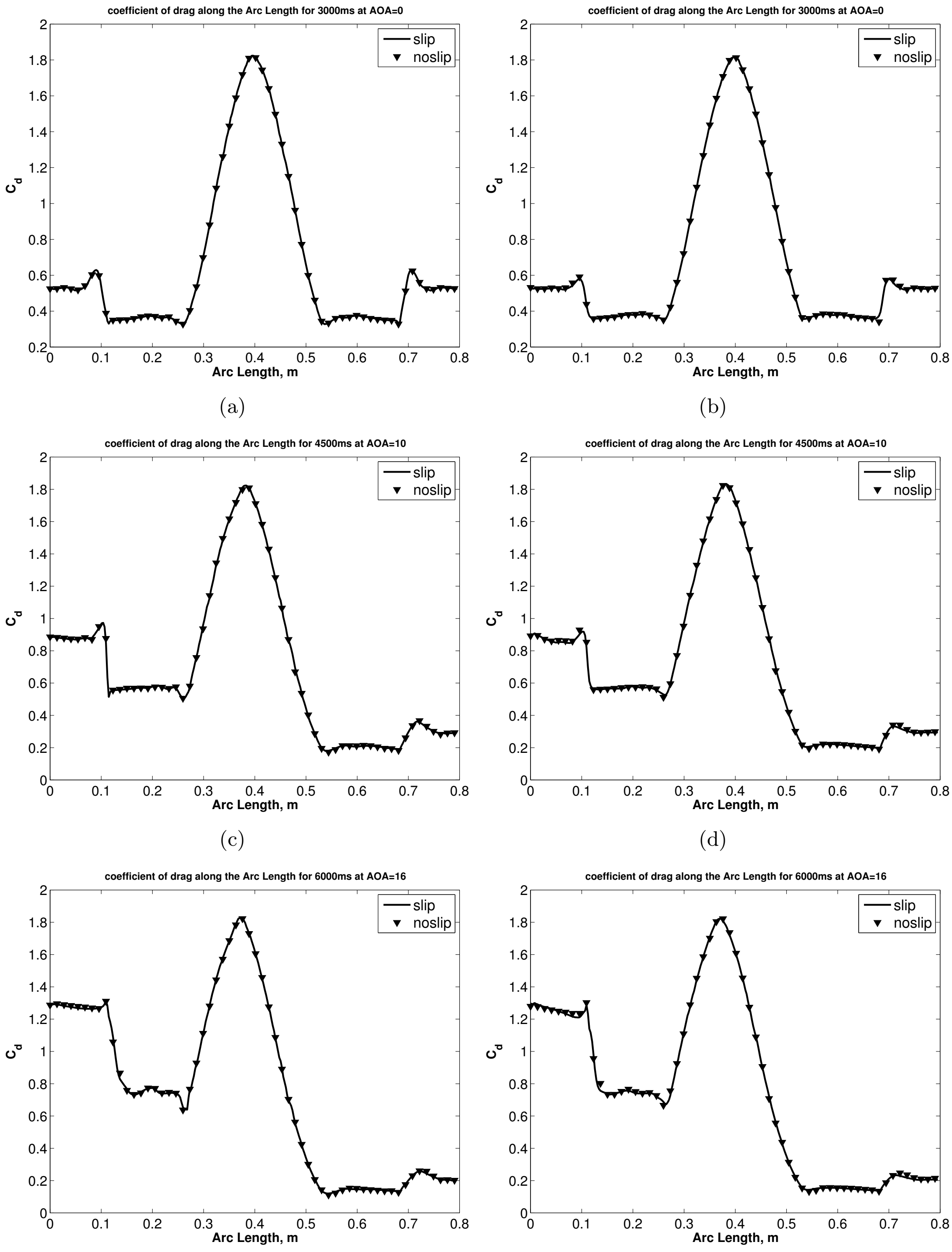

(a) (b)

(c) (d)

(e) (f)

Figure 5.4: Drag coefficient comparison on the capsule surface at different altitudes with variation of speed for different angles of attack (a) Variation of at 60km and 3000m/s. (b) 70km and 3000m/s. (c) 60km and 4500m/s (d) 70km and 4500m/s (e) 60km and 6000m/s (f) 70km and 6000m/s

%Deviation - Coefficient of local heat transfer				
60km				
Angle of attack	0	10	16	20
3000(m/s)	6.6217	6.6616	6.3559	5.9733
4500(m/s)	18.1593	18	17.7526	15.5651
6000(m/s)	29.4956	29.1987	28.8346	25.6175
70km				
Angle of attack	0	10	16	20
3000(m/s)	7.7729	7.5060	7.0581	4.8917
4500(m/s)	24.0827	23.7214	23.1103	18.7343
6000(m/s)	37.2991	36.8470	36.1479	35.5677

Table 5.2: Percentage deviation in Coefficient of local heat transfer

5.3 Slip and Jump Phenomena

Temperature jump as well as axial slip velocity increases as altitude increases and also it is high for higher Mach number. But change of axial slip velocity with Mach number is not as significant as that for temperature jump, this is due to the fact that non-equillibrium nature for momentum transfer is simply governed by Knudsen number i.e. altitude variation while non equillibrium nature for energy transfer is governed by Knudsen number as well as Mach number. That we can see from Fig. 5.6 and Fig. 5.7 On windward side of capsule temperature jump is lower compared to leeward side as angle of attack increases. At 20 AOA flow is smooth on windward side therefore normalized temperature jump is almost constant approx 1 on windward side. Axial slip velocity does not affect much with speed except at sharp features like cone section On windward side of capsule axial slip is lower compared to leeward side as angle of attack increases. And at 20 AOA it is approximately constant on windward side. But as angle of attack increases both temperature jump and axial slip velocity increases on leeward side as density of particle is lower on leeward side.

Radial slip does not changes much with speed as the same reason for axial slip. And is negative on windward side and positive on leeward side. Magnitude of radial slip is Higher at higher altitude as non-equillibrium nature of radial momentum transfer due to altitude change. Radial slip increases with increase in angle of attack and magnitude of radial slip increases on leeward side as angle of attack increases as particles will have more space for collision on leeward side.

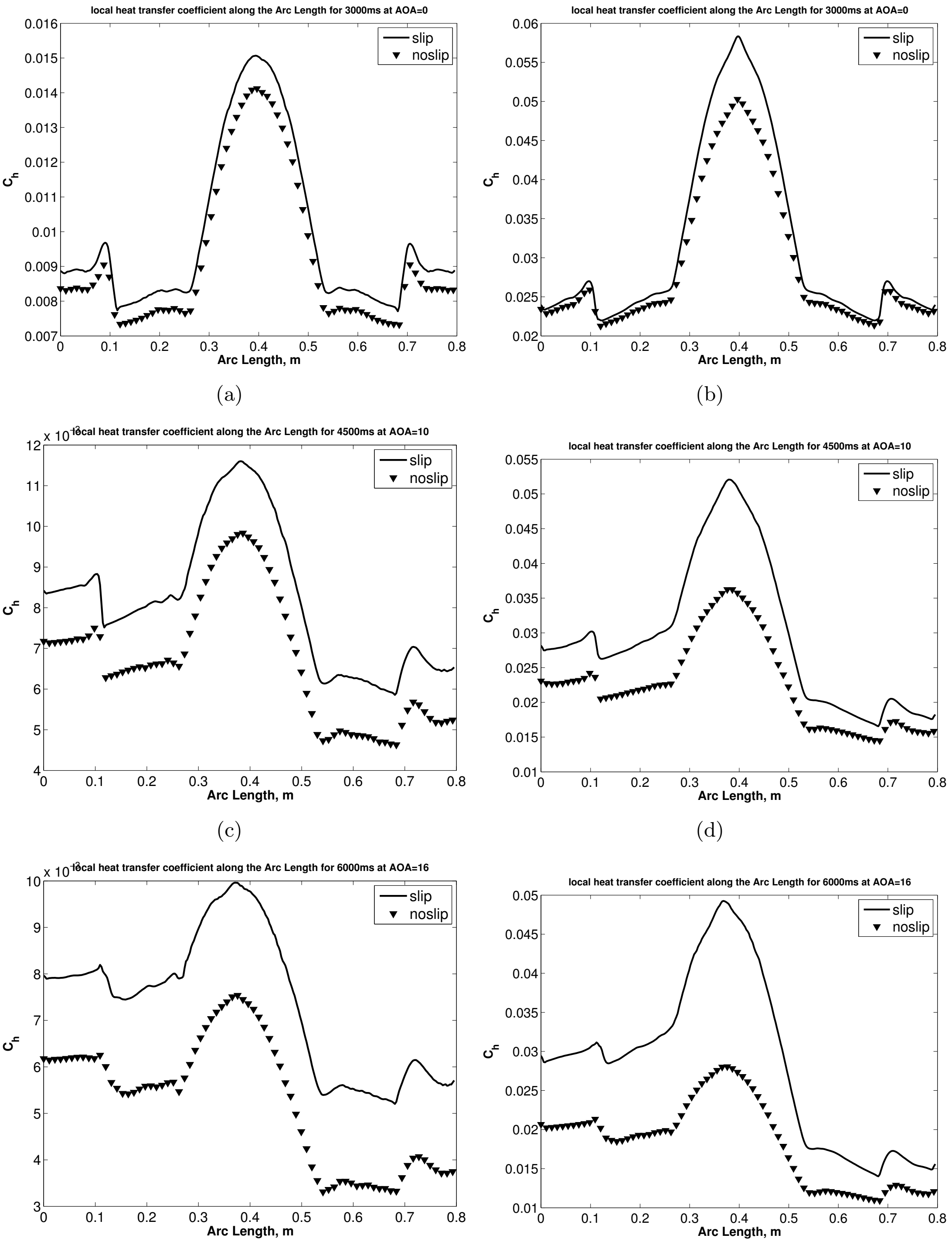

(a) (b) (c) (d) (e) (f)

Figure 5.5: Heat transfer coefficient comparison on the capsule surface at different altitudes with variation of speed for different angles of attack (a) Variation of at 60km and 3000m/s. (b) 70km and 3000m/s. (c) 60km and 4500m/s (d) 70km and 4500m/s (e) 60km and 6000m/s (f) 70km and 6000m/s

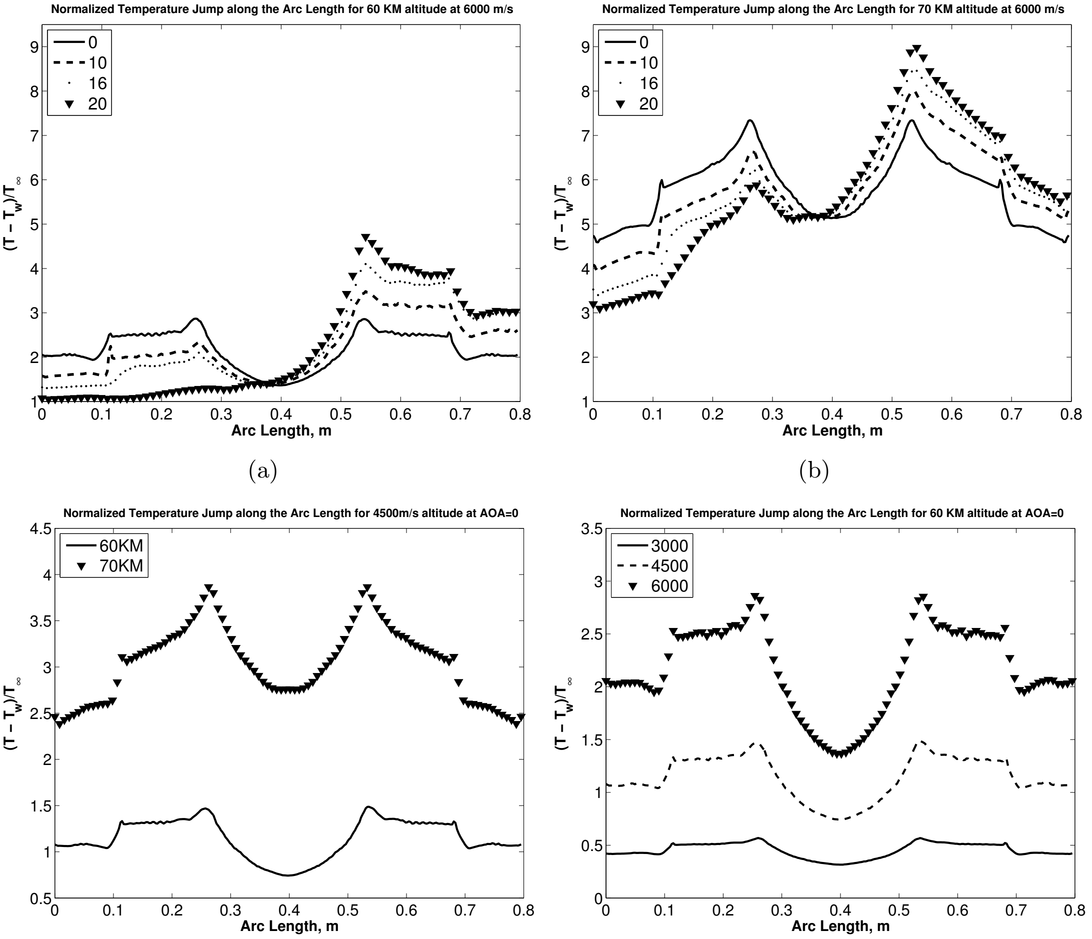

(a) (b)

(c) (d)

Figure 5.6: Temperature jump on the capsule surface at different altitudes with variation of speed for different angles of attack (a) Variation of angles of attack at 60km and 6000m/s. (b) Variation of angles of attack at 70km and 6000m/s., (c) Variation of altitude at 4500m/s and 0 AOA (d) At different Mach Numbers.

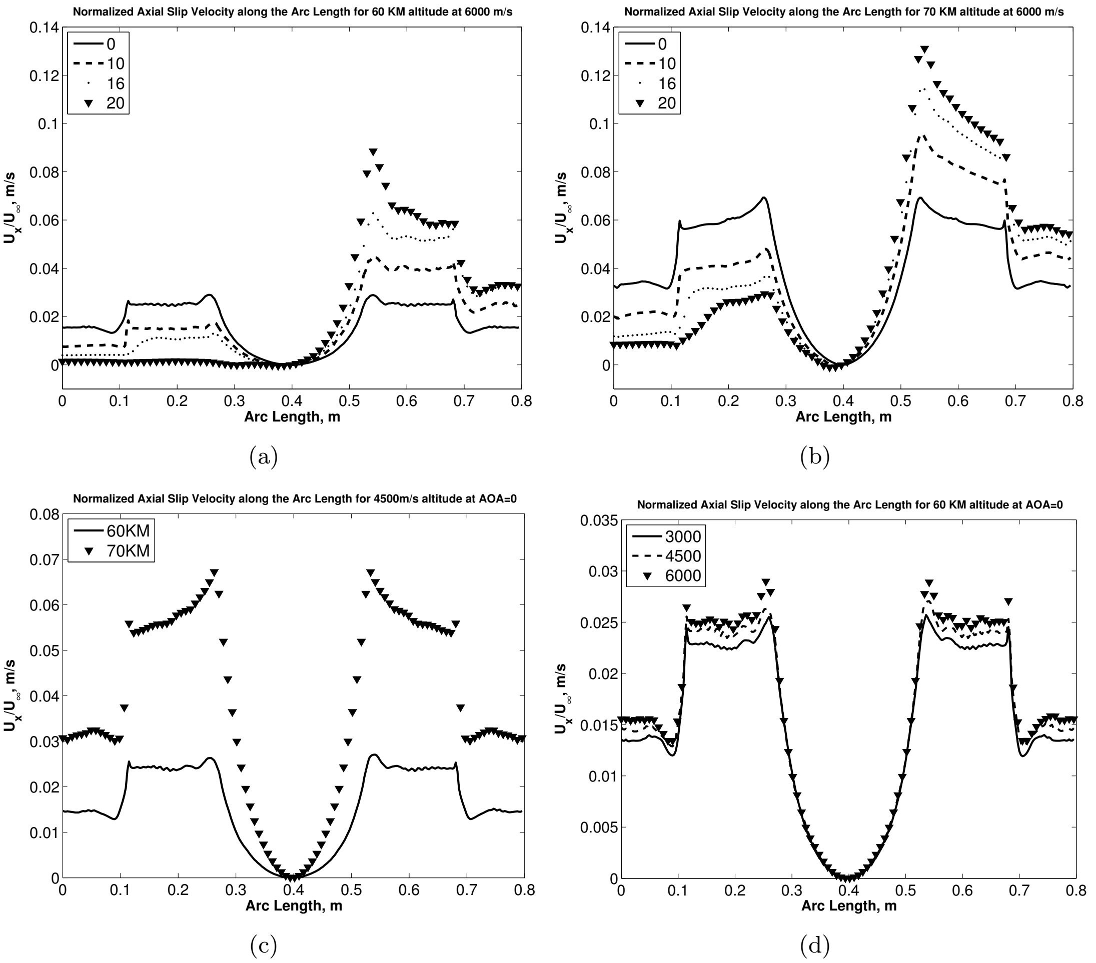

Figure 5.7: Axial Slip Velocity on the capsule surface at different altitudes with variation of speed for different angles of attack (a) Variation of angles of attack at 60km and 6000m/s. (b) Variation of angles of attack at 70km and 6000m/s, (c) Variation of altitude at 4500m/s and 0 AOA (d) At different Mach Numbers.

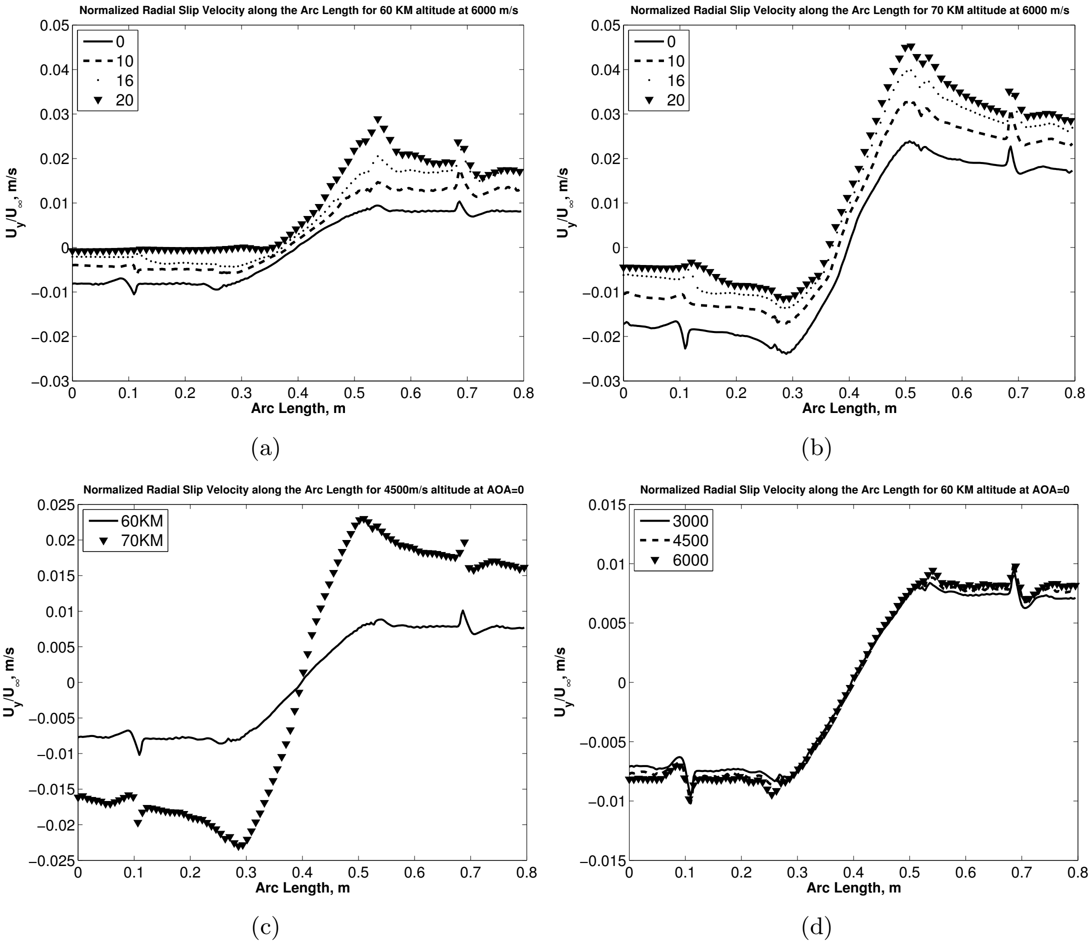

(a) (b)

(c) (d)

Figure 5.8: Radial Slip Velocity on the capsule surface at different altitudes with variation of speed for different angles of attack (a) Variation of angles of attack at 60km and 6000m/s. (b) Variation of angles of attack at 70km and 6000m/s, (c) Variation of altitude at 4500m/s and 0 AOA (d) At different Mach Numbers.

Chapter 6

Conclusion and Future Work

I have presented non-equilibrium aero-thermodynamic characteristics of rarefied gas flow over the bi-conical re-entry capsule in the slip flow regime. The numerical simulations are carried out with continuum methods. Both the no-slip/no-jump and the first-order slip/jump/transpiration boundary conditions are implemented in the CFD method. The open source software OpenFOAM is used for both CFD methods, and they are validated with the experimental data for 33 km altitude conditions. It is also tested with flat plate and wedge case experimental data. Pressure on wall well agrees with experimental data but velocity underpredicts the results. And also CFD method are very sensitive at sharp geometries due to nonequillibrium effect produced by thicknesss of plate I have carried out detailed investigations to report the non-equilibrium effects on the drag, and heat transfer coefficients by comparing the conventional and slip CFD results.

I have compared the results for single-cone and bi-cone configuration keeping cone angle and axial length same. There is an increase in the values of drag coefficient but decrease in values of heat transfer coefficient when changed configuration from single-cone to bi-cone. But reduction in heat transfer coefficient is around 35% which is much significant on the other hand increase in drag coefficient is not more than 5%. We can accomodate 4-5% deviation in drag coefficient and can say bi-cone configuration is more aerothermodyanamically optimized configuration than single-cone.

The CFD results for drag coefficients found good agreement. However, the heat transfer coefficients comparisons reveal that the non-equilibrium description of energy transfer depends on both the Knudsen number and Mach number. The rotational energy transfer is more pronounced with increase in Mach number, although the simulated Knudsen numbers are in the early slip flow regime. This is also evident from the normalized slip velocity and temperature jump results, that the amount of normalized slip is negligible when compared to the normalized temperature jump, especially with increase in Mach number.

Hence, the accuracy of theoretical/continuum models for high-speed re-entry gas flow in the slip and transition flow regions cannot be decided based upon the mere comparisons for drag and pressure coefficients, which are usually reported by experiments. Heat/energy transfer plays key role in determining the deficiencies in the classical continuum methods for high-speed rarefied gas flows. Although the current test cases are in the early slip flow regime, the first-order non-equilibrium boundary conditions are not sufficient to accurately describe the non-equilibrium gas flow physics. We may need to incorporate both the higher-order boundary conditions as well as the non-linear constitutive relations into the Navier-Stokes equations framework to report better predictions for re-entry gas flows. This can be done as a future work to this current work This is very important from the numerical simulations perspective as particle methods are still computationally intensive for simple gas flows and indeed expensive for 3-D complex geometries.

Appendices

Appendix A

Boundary Conditions

Following is part of openFoam code that shows how to incorporate Maxwellian slip and smoluchowski boundary condition and turbulence modelling in solver.

A.1 Velocity Boundary Condition

```
boundaryField

    OBSTACLE

    type maxwellSlipU;
    refValue uniform (0 0 0);
    valueFraction uniform 0;
    accommodationCoeff 0.9;
    Uwall uniform (0 0 0);
    thermalCreep true;
    curvature true;
    value uniform (0 0 0);
```

A.2 Temperature Boundary Condition

```
boundaryField

    OBSTACLE
```

```
     type    smoluchowskiJumpT;
     Twall   uniform   550;
     accommodationCoeff  1;
```

A.3 Turbulence Modelling

```
fluxScheme      Tadmor;

ddtSchemes

    default          Euler;



gradSchemes

    default          Gauss linear;


divSchemes

    default         none;
    div(tauMC)      Gauss linear;
    div(phi,nuTilda) Gauss Gamma 1;
    div(phi,k) Gauss Gamma 1;
    div(phi,epsilon) Gauss Gamma 1;
    div(phi,omega) Gauss Gamma 1;


laplacianSchemes

    default         Gauss linear corrected;
```

```
interpolationSchemes

    default         linear;
    reconstruct(rho) Gamma 1;
    reconstruct(U)  GammaV 1;
    reconstruct(T)  Gamma 1;


snGradSchemes

    default         corrected;


ddtSchemes

    default         Euler;


gradSchemes

   default         Gauss linear;
   grad(U) Gauss linear;
   grad(rho) Gauss linear;
   grad(rhoU) Gauss linear;
   grad((1|psi)) Gauss linear;
   grad(e) Gauss linear;
   grad(sqrt(((Cp|Cv)*(1|psi)))) Gauss linear;
   grad(c) Gauss linear;
   grad(T) Gauss linear;
   grad(epsilon) Gauss linear;
   grad(k) Gauss linear;


divSchemes

    default         none;
    div(tauMC)      Gauss linear;
    div(phi) Gauss linear;
    div(phi,epsilon) Gauss linear;
```

```
    div(phi,k) Gauss linear;
    div(phiEp) Gauss linaer;
    div(phiUp) Gauss linear;
    div(sigmaDotU) Gauss linear;


laplacianSchemes

    default         Gauss linear corrected;
    laplacian(muEff,U) Gauss linear corrected;
    laplacian(alphaEff,e) Gauss linear corrected;
    laplacian(alpha,e) Gauss linear corrected;
    laplacian(k,T) Gauss linear corrected;
    laplacian(DepsilonEff,epsilon) Gauss linear corrected;
    laplacian(DkEff,k) Gauss linear corrected;


interpolationSchemes

    default         linear;
    reconstruct(rho) vanLeer;
    reconstruct(U)  vanLeerV;
    reconstruct(T)  vanLeer;
    interpolate(rho) linear;
    interpolate(U) linear;
    interpolate(T) linear;
    interpolate(e) linear;
    interpolate(c) linear;
    interpolate(rhoU) linear;
    interpolate(rPsi) linear;
    interpolate(muEff) linear;
    interpolate(tauMC) linear;


snGradSchemes

    default         corrected;

    snGrad(U) corrected;
```

```
*/


// ************************************************************************* //

solvers

    rho

        solver          diagonal;



    rhoU

        solver          diagonal;



    rhoE

        solver          diagonal;



    U

        solver          smoothSolver;
        smoother        GaussSeidel;
        nSweeps         2;
        tolerance       1e-10;
        relTol          0;



    e

        solver          smoothSolver;
        smoother        GaussSeidel;
        nSweeps         2;
        tolerance       1e-10;
```

```
    relTol          0;


nuTilda

    solver          smoothSolver;
    smoother        GaussSeidel;
    nSweeps         2;
    tolerance       1e-10;
    relTol          0;


k

    solver          smoothSolver;
    smoother        GaussSeidel;
    nSweeps         2;
    tolerance       1e-10;
    relTol          0;


epsilon

    solver          smoothSolver;
    smoother        GaussSeidel;
    nSweeps         2;
    tolerance       1e-10;
    relTol          0;


omega

    solver          smoothSolver;
    smoother        GaussSeidel;
    nSweeps         2;
    tolerance       1e-12;
    relTol          0;
```

```
/*solvers

    "(rho|rhoU|rhoE)"

        solver          diagonal;


    "(U|e)"

        solver          smoothSolver;
        smoother        GaussSeidel;
        nSweeps         2;
        tolerance       1e-09;
        relTol          0.01;


    h

        $U;
        tolerance       1e-10;
        relTol          0;

    "(k|epsilon)"

solver smoothSolver;
smoother GaussSeidel;
nSweeps 2;
tolerance 1e-09;
relTol 0;


*/

// ************************************************************************* //
```

References

[1] R. D. Launius and D. R. Jenkins. Coming Home: Reentry and Recovery from Space. Government Printing Office, 2012.

[2] B. John, D. Mathew, B. Deependran, G. Joseph, C. R. Nair, and K. Ninan. Medium-density ablative composites: processing, characterisation and thermal response under moderate atmospheric re-entry heating conditions. *Journal of Materials Science* 46, (2011) 5017–5028.

[3] M. Sippel, T. Schwanekamp, O. Trivailo, and A. Lentsch. Progress of SpaceLiner Rocket-Powered High-Speed Concept. In 64th International Astronautical Congress. 2013 .

[4] T. Schwanekamp, F. Meyer, T. Reimer, I. Petkov, A. Tröltzsch, and M. Siggel. System Studies on Active Thermal Protection of a Hypersonic Suborbital Passenger Transport Vehicle .

[5] W. Hohmann. Die Erreichbarkeit der Himmelskörper. Untersuchungen über das Raumfahrtproblem. *Die Erreichbarkeit der Himmelskörper. Untersuchungen über das Raumfahrtproblem., by Hohmann, W.. Oldenbourg, München (Germany), 1994, 122 p., ISBN 3-486-23106-5, Price DM 29.80.* 1.

[6] F. Clauser. Preliminary Design of an Experimental World-Circling Spaceship. Douglas Aircraft Company Engineering Division, 1946.

[7] J. C. Ross, J. T. Heineck, N. Burnside, M. E. Sellers, N. Halcomb, T. Garbeff, G. Yamauchi, and L. Kushner. Comprehensive Study of the Flow Around a Simplified Orion Capsule Model. In 31st AIAA Applied Aerodynamics Conference. American Institute of Aeronautics and Astronautics. 00004.

[8] M. Lighthill. Dynamics of a dissociating gas. Part I. Equilibrium flow. *J. Fluid Mech* 2, (1957) 1–32.

[9] P. A. Liever, S. D. Habchi, S. I. Burnell, and J. S. Lingard. Computational fluid dynamics prediction of the Beagle 2 aerodynamic database. *Journal of spacecraft and rockets* 40, (2003) 632–638.

[10] R. Mehta. Numerical simulation of supersonic flow past reentry capsules. *Shock Waves* 15, (2006) 31–41.

[11] R. Deissler. An analysis of second-order slip flow and temperature-jump boundary conditions for rarefied gases. *International Journal of Heat and Mass Transfer* 7, (1964) 681–694.

[12] C. Cercignani. Higher order slip according to the linearized Boltzmann equation. Technical Report, DTIC Document 1964.

[13] D. A. Lockerby, J. M. Reese, and M. A. Gis. The usefulness of higher-order constitutive relations for describing the Knudsen layer. *Physics of Fluids (1994-present)* 17, (2005) 100,609.

[14] D. A. Lockerby and J. M. Reese. On the modelling of isothermal gas flows at the microscale. *Journal of Fluid Mechanics* 604, (2008) 235–261.

[15] N. G. Hadjiconstantinou. The limits of Navier-Stokes theory and kinetic extensions for describing small-scale gaseous hydrodynamics. *Physics of Fluids (1994-present)* 18, (2006) 111,301.

[16] N. Dongari, Y. Zhang, and J. M. Reese. Modeling of Knudsen layer effects in micro/nanoscale gas flows. *Journal of Fluids Engineering* 133, (2011) 071,101.

[17] R. Votta, A. Schettino, A. Bonfiglioli, D. A. Levin, I. J. Wysong, and A. L. Garcia. Advanced Models for Prediction of High Altitude Aero-Thermal Loads of a Space Reentry Vehicle. In AIP Conference Proceedings-American Institute of Physics, volume 1333. 2011 1343.

[18] G. Ranuzzi and S. Borreca. CLAE project. H3NS: Code development verification and validation. Technical Report, CIRA-CF-06-1017 2006.

[19] B. R. Hollis, K. T. Berger, S. A. Berry, G. J. Brauckmann, G. M. Buck, M. DiFulvio, T. J. Horvath, D. S. Liechty, N. Merski, K. J. Murphy et al. Entry, Descent and Landing Aerothermodynamics: NASA Langley Experimental Capabilities and Contributions .

[20] R. Votta, A. Schettino, G. Ranuzzi, and S. F. Borrelli. Hypersonic low-density aerothermodynamics of Orion-like exploration vehicle. *Journal of Spacecraft and Rockets* 46, (2009) 781–787.

[21] C. J. Greenshields, H. G. Weller, L. Gasparini, and J. M. Reese. Implementation of semi-discrete, non-staggered central schemes in a colocated, polyhedral, finite volume framework, for high-speed viscous flows. *International journal for numerical methods in fluids* 63, (2010) 1–21.

[22] A. Bansal, A. Feldick, and M. Modest. Simulation of Hypersonic Flow and Radiation over a Mars Reentry Vehicle Using OpenFOAM. In 50th AIAA Aerospace Sciences Meeting including the New Horizons Forum and Aerospace Exposition: ISBN. 2012 978–1.

[23] S. Nakao, M. Kashitani, T. Miyaguni, and Y. Yamaguchi. A study on high subsonic airfoil flows in relatively high Reynolds number by using OpenFOAM. *Journal of Thermal Science* 23, (2014) 133–137.

[24] P. SPALART and S. ALLMARAS. A one-equation turbulence model for aerodynamic flows. In 30th Aerospace Sciences Meeting and Exhibit, Aerospace Sciences Meetings. American Institute of Aeronautics and Astronautics, 1992. 05351.

[25] B. E. Nikaido, S. M. Murman, and J. Garcia. OpenFOAM Simulations of Atmospheric-Entry Capsules in the Subsonic Regime. In 53rd AIAA Aerospace Sciences Meeting, AIAA SciTech. American Institute of Aeronautics and Astronautics, 2015. 00000.

[26] J. C. Maxwell. On Stresses in Rarefied Gases Arising from Inequalities of Temperature. *Proceedings of the Royal Society of London* 27, (1878) 304–308.

[27] N. T. Le, C. White, J. M. Reese, and R. S. Myong. Langmuir–Maxwell and Langmuir–Smoluchowski boundary conditions for thermal gas flow simulations in hypersonic aerodynamics. *International Journal of Heat and Mass Transfer* 55, (2012) 5032–5043.

[28] A.-M. Mahdavi, N. T. Le, E. Roohi, and C. White. Thermal Rarefied Gas Flow Investigations Through Micro-/Nano-Backward-Facing Step: Comparison of DSMC and CFD Subject to Hybrid Slip and Jump Boundary Conditions. *Numerical Heat Transfer, Part A: Applications* 66, (2014) 733–755.

[29] N. Le, C. J. Greenshields, and J. Reese. Evaluation of nonequilibrium boundary conditions for hypersonic rarefied gas flows. In Progress in Flight Physics, volume 3. EDP Sciences, 2012 217–230.

[30] E. B. Arkilic, M. A. Schmidt, and K. S. Breuer. Gaseous slip flow in long microchannels. *Microelectromechanical Systems, Journal of* 6, (1997) 167–178.

[31] S. Colin. Rarefaction and compressibility effects on steady and transient gas flows in microchannels. *Microfluidics and Nanofluidics* 1, (2005) 268–279.

[32] M. Gad-el Hak. The fluid mechanics of microdevicesthe Freeman scholar lecture. *Journal of Fluids Engineering* 121, (1999) 5–33.

[33] G. Bird. Molecular Gas Dynamics and the Direct Simulation of Gas Flows. Number v. 1 in Molecular Gas Dynamics and the Direct Simulation of Gas Flows. Clarendon Press, 1994.

[34] B. S. Baldwin and H. Lomax. Thin layer approximation and algebraic model for separated turbulent flows, volume 257. American Institute of Aeronautics and Astronautics, 1978.

[35] D. Degani and L. Schiff. Computation of supersonic viscous flows around pointed bodies at large incidence. National Aeronautics and Space Administration, Ames Research Center, 1983.

[36] P. Spalart and S. Allmaras. A One-Equation Turbulence Model for Aerodynamic Flows. AIAA-Paper 92-0439, 1992. In 30th Aerospace Sciences Meeting & Exhibit, Jan 6–9.

[37] P. Spalart and M. Shur. On the sensitization of turbulence models to rotation and curvature. *Aerospace Science and Technology* 1, (1997) 297–302.

[38] C. Gacherieu, C. Weber, and G. Coriolis. Assessment of algebraic and one-equation turbulence models for the transonic turbulent flow around a full aircraft configuration. *AIAA paper* 98–32,457.

[39] S. Deck, P. Duveau, P. d'Espiney, and P. Guillen. Development and application of Spalart–Allmaras one equation turbulence model to three-dimensional supersonic complex configurations. *Aerospace Science and Technology* 6, (2002) 171–183.

[40] A. J. Lofthouse. Nonequilibrium hypersonic aerothermodynamics using the direct simulation Monte Carlo and Navier-Stokes models. ProQuest, 2008.

[41] S. Nagdewe, G. Shevare, and H.-D. Kim. Study on the numerical schemes for hypersonic flow simulation. *Shock Waves* 19, (2009) 433–442.

[42] R. Kalimuthu. Surface Pressure Measurement Results on the SRE (biconic) Configuration at Mach= 5. Vikram Sarabhai Space Center. Technical Report, Internal Rept. VSSC/ATFD/TM_SRE/078/2003, Thiruvananthpuram, India 2003.